

Physical Properties and Thermal Stability of Zirconium Platinum Nitride Thin Films

R.A. Gallivan,¹ J. Manser,¹ A. Michelini,¹ N. Toncich,¹ N. Abando Beldarrain,¹ C. Vockenhuber,² A. Müller,² and H. Galinski¹

¹Laboratory for Nanometallurgy, Department of Materials, ETH Zurich

²Ion Beam Physics, Department of Physics, ETH Zurich

(*Electronic mail: henning.galinski@mat.ethz.ch)

(*Electronic mail: rebecca.gallivan@mat.ethz.ch)

(Dated: 26 July 2024)

Ternary transition metal nitrides (TMNs) promise to significantly expand the material design space by opening new functionality and enhancing existing properties. However, most systems have only been investigated computationally and limited understanding of their stabilizing mechanisms restricts translation to experimental synthesis. To better elucidate key factors in designing ternary TMNs, we experimentally fabricate and analyze the physical properties of the ternary Zr-Pt-N system. Structural analysis and DFT modeling demonstrate that Pt substitutes nitrogen on the non-metallic sublattice, which destabilizes the rock-salt structure and forms a complex cubic phase. We also show insolubility of Pt in the Zr-Pt-N at 45 at% with the formation of a secondary Pt-rich phase. The measured reduced plasma frequency, decrease in resistivity, and decrease in hardness reflect a dominance of metallic behavior in bonding. Contrary to previous computational predictions, Zr-Pt-N films are shown to be metastable systems where even low Pt concentrations (1%) facilitate a solid reaction with the Si-substrate, that is inaccessible in ZrN films.

Transition metal nitrides (TMNs) are a peculiar class of interstitial compounds, where nitrogen forms a non-metallic sublattice on the interstitial sites of the crystal. These materials can assume metallic, ionic, and covalent behavior at the same time because of their unique combination of a finite density of states (DOS) at the Fermi energy, wave-function overlap, and electrostatic interactions between the metallic and non-metallic sublattice. Depending on the DOS, stoichiometry, and defects in these sublattices, TMNs can reach diamond-like hardness¹⁻³, high melting-points^{4,5}, plasmonic dispersion⁶, high carrier mobility^{7,8}, catalytic activity^{9,10}, magneto-ionic cyclability¹¹ and superconductivity¹². This versatility coupled with the CMOS-compatibility of nitrides such as ZrN, TiN, and HfN offers great potential for conventional and quantum applications.

While binary TMNs are widely studied, ternary TMNs remain largely unexplored. Existing experimental work like that on ZnZrN¹³ and TiAlN¹⁴ highlight a key challenge of producing stable rather than metastable ternary TMNs. Furthermore the large potential alloying space and limited insights to stabilizing mechanisms complicate materials selection for designing new ternary TMNs. Recent advances in high throughput material screening¹⁵ help circumvent these challenges and enable density functional theory (DFT) calculated stability maps like the one introduced by Sun *et al.*¹⁶. Although these DFT simulations provide promising evidence for the stability of a large variety of ternary metal nitrides¹⁶, few of these systems have been experimentally fabricated or characterized.

In particular, the Zr-Pt-N system shows promise for functional enhancements in catalytic properties by the incorporation of a highly active metal like platinum. ZrN itself has strong catalytic properties with a recent study showing that

ZrN nanoparticles can outperform Pt in alkaline solutions⁹. Similarly Zr-oxynitrides demonstrate strong catalytic activity as shown through oxygen reduction reaction (ORR) measurements in acid media^{17,18} and exhibit high oxygen diffusivity¹⁹. These properties make them a good candidate for a mixed ionic-electronic conductor. Thus, introducing platinum, a highly active metal, may provide even greater functional enhancements which are critical to applications from thermophotovoltaics to fuel cells and plasmon enhanced chemistry. Despite its potential as a functional material, Zr₄Pt₂N₃'s structure and properties have only been reported computationally²⁰ and no experimental synthesized Zr-Pt-N systems are known.

In this study, we fabricate and explore the ternary nitride Zr-Pt-N with special emphasis on the effect of an increasing Pt-content on phase stability and optical, mechanical, and electrical properties. Through magnetron sputtering, we deposit ZrPt_xN_y as films with varying concentrations of Pt. The structure and functional properties of these new Zr-Pt-N films are compared to the binary nitride counterpart, ZrN, a common nitridic material with a high melting temperature (2900°C)⁴, high mechanical durability and hardness (23 to 30 GPa)¹⁻³, and similar electrical resistivity to its metallic counterpart^{7,8}.

To link the evolution of the physical properties to changes in chemistry, it is important to get insights into the atomic structure of these complex ternary nitrides. For this purpose, it is convenient to assume mono-crystalline and defect-free materials as a reference since their atomic structure is computationally available using first-principle techniques. Figure 1a depicts the optimized crystal structure of ZrN and Zr₁₆Pt₆N₆ calculated with Quantum Espresso²¹. Here, ZrN forms a rock-salt structure with four atoms per unit cell. With the addition

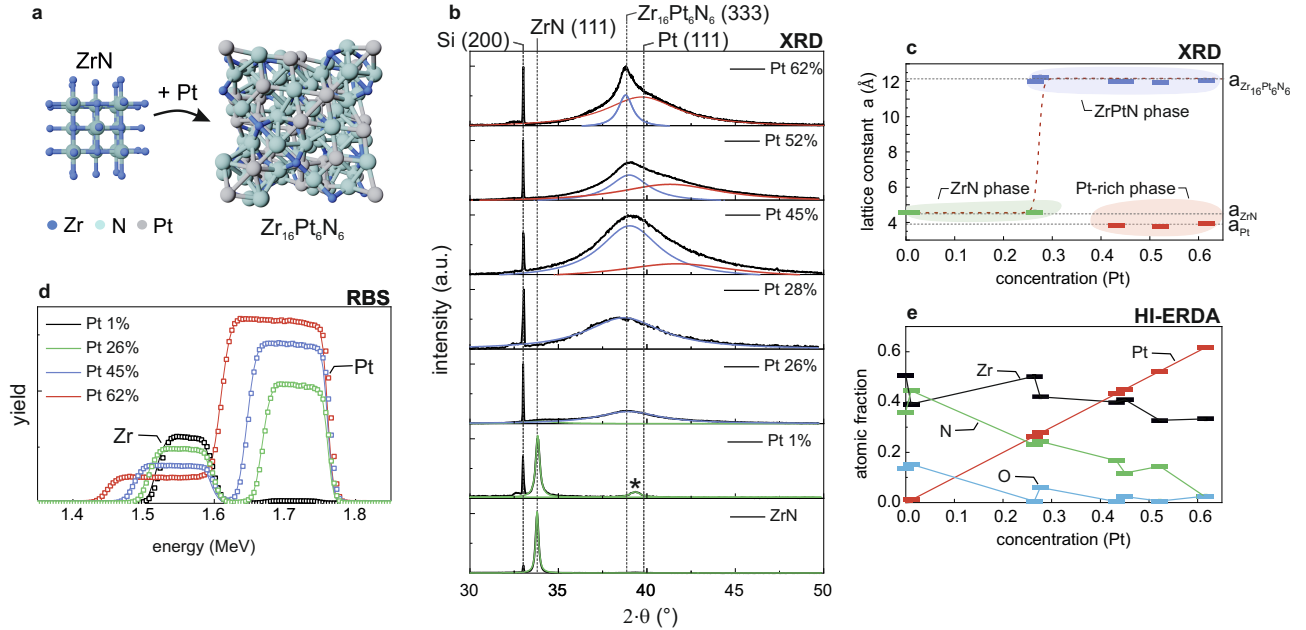


FIG. 1. Phase Formation. (a) Transition of the crystal structure from ZrN (rock-salt) to $Zr_{16}Pt_6N_6$ (diamond-like) due to the addition of Pt. Depicted crystal structures are based on fully-relaxed DFT calculations. (b) XRD spectra of $ZrPt_xN_y$ thin films with increasing Pt concentration (0 – 62%). Deconvoluted peaks correspond to the ZrN-phase (green), the ZrPtN-phase (blue) and secondary Pt nuclei (red). The annotated $Zr_{16}Pt_6N_6$ (333) peak has been derived from DFT calculations. * denotes the (200) belonging to ZrN. Co-existence of ZrN phase and $Zr_{16}Pt_6N_6$ occurs at Pt= 26%. (c) Calculated lattice constants as a function of Pt concentration. Literature/DFT-based values are annotated at the right side. (d) RBS spectra of selected ZrPtN films with increasing Pt-content showing high uniformity. (e) Evolution of the film chemistry as a function of Pt concentration based on elastic recoil detection analysis with heavy ions (HI-ERDA).

of Pt atoms, the unit cell expands to 28 atoms/cell and forms a stable diamond-like structure. This aligns with previous DFT calculations reported in the literature^{16,20}.

The experimental structural and chemical data based on Rutherford backscattering (RBS)²², X-ray diffraction (XRD), and elastic recoil detection analysis with heavy ions (HI-ERDA)²² presented in Figure 1 identify the formation of a distinct $ZrPt_xN_y$ phase where Pt substitutes on the N sublattice sites. At low Pt concentrations ($\leq 1\%$) the film maintains the rock-salt structure typical of ZrN (green peak) and simply incorporates Pt as a defect (Figure 1b). However, at larger concentrations of Pt, the $ZrPt_xN_y$ peak (blue) appears and the material shifts to a new cubic unit cell with a lattice parameter of 12 Å (Figure 1c). For films with a high concentration of Pt ($\geq 45\%$), a second peak emerges (red). Based on the lattice parameter calculations highlighted in Figure 1c, this broad peak is associated with a distinct Pt-rich phase. The extensive peak broadening suggests that the Pt forms very small (< 1 nm) and finely dispersed crystalline nuclei.

As Pt is introduced, it substitutes on the N site due to the strong bonding interaction between Zr and Pt²³. While predicted computationally, this Pt substitution of N is also observed experimentally using HI-ERDA as increases in Pt content correspond to equivalent decreases in N content (Figure 1e). Zr remains at a fairly consistent atomic fraction inde-

pendent of Pt concentration. Oxygen content also decreases from 0.15 to less than 0.03 atomic fraction with increasing Pt content. The oxygen content observed is mostly attributed to surface oxidation based on the localization observed in the HI-ERDA results (see Supplementary Information). RBS measurements shown in Figure 1d confirm the chemical uniformity of the sputter deposited films.

We characterize the optical response of the ternary metal nitrides for different Pt concentration via ellipsometry and near-normal incidence reflectometry. Figure 2 highlights the control in optical property through the alloying of Pt in these ternary nitridic films. Addition of Pt flattens the real part of the film's permittivity ϵ and shifts the crossover frequency to the metallic regime, i.e. $\Re\epsilon(\omega_p)$, further into the UV (Figure 2a). Simultaneously, the imaginary part of the permittivity, i.e. the optical loss, increases as function of Pt content for all wavelengths (Figure 2b). The extension of the metallic regime is also featured in the materials reflectance (Figure 2c). Under near-normal reflectance, the addition of Pt increases reflectance at all wavelengths but with particular increase at wavelengths below 600 nm. For Pt concentrations $\geq 26\%$, the films form a broadband reflector. While the response of ZrN is still dominated by interband transition that lead to the formation of a characteristic absorption edge and goldish coloration²⁶, the addition of Pt changes the band structure and

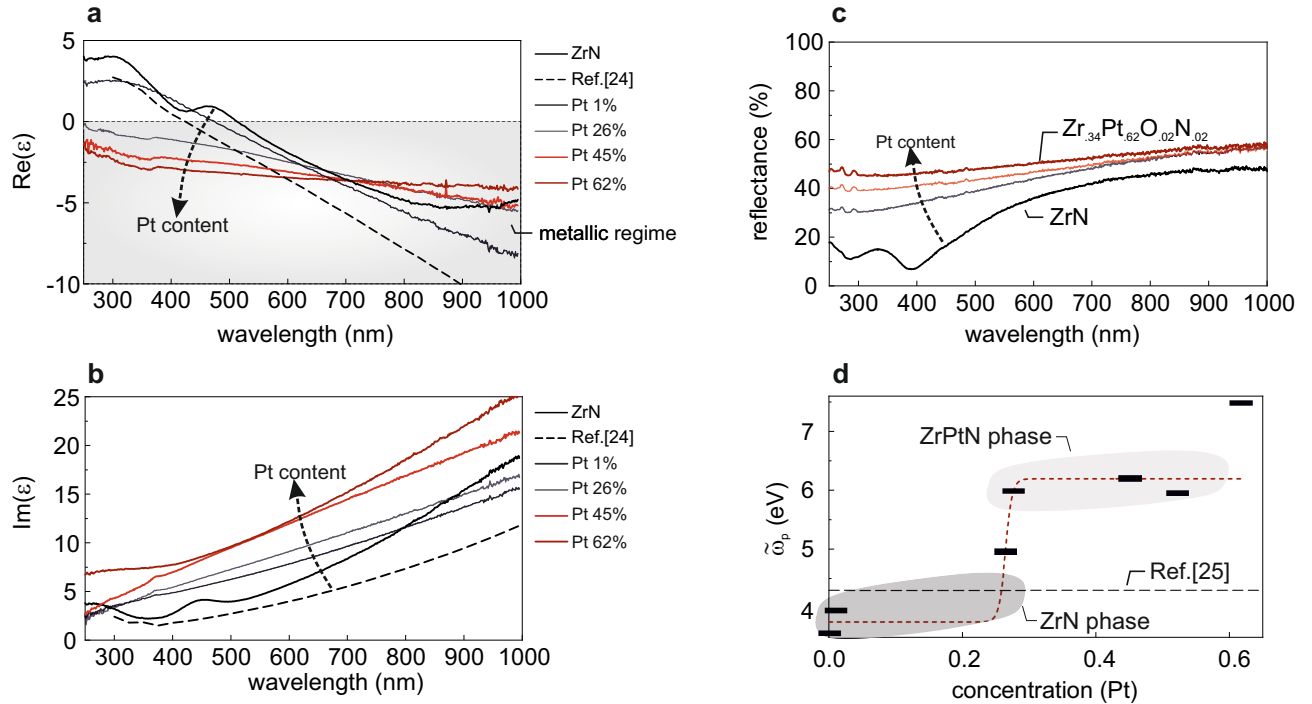


FIG. 2. Optical Properties. (a) Real and (b) imaginary part of the dielectric function for five examined ZrPt_xN_y films in the as-deposited state and compared to ZrN data from literature²⁴. Substitution of N with Pt on the nitrogen sublattice continuously blue-shifts the metallic regime i.e. $\text{Re}(\epsilon) < 0$. (c) Near-normal incidence reflectance spectra of four selected ZrPt_xN_y films with increasing Pt-content. (d) Reduced plasma frequency ($\tilde{\omega}_p$) versus Pt-content. $\tilde{\omega}_p$ is obtained by fitting the experimentally measured permittivity from (a) and (b) using a Drude-Lorentz model. The step-like increase reflects both, the significant increase in free carrier concentration with increasing Pt-content and the crystallographic phase-transition from observed by XRD. The effective plasma frequency of ZrN from Ref.²⁵ is plotted for comparison.

consequently the optical transitions significantly.

To quantify this transition, we parameterize the complex permittivity with a finite set of Drude-Lorentz (DL) oscillators²⁷. The DL model takes into account the effective mass m^* of the charge carriers and is suited to represent interband transitions. The crossover frequency to the metallic regime is given by the reduced plasma $\tilde{\omega}_p = \omega_p / \sqrt{\epsilon_\infty} = \sqrt{ne^2 / m^* \epsilon_\infty}$, which mainly depends on the ratio of the background permittivity ϵ_∞ and the density of carriers n taking part in the transition. Figure 1d presents the screened plasma frequency $\tilde{\omega}_p$ as a function of Pt concentration. For ZrPt_xN_y phases, $\tilde{\omega}_p$ increases more than 2-fold from 3.6 eV in ZrN to 5.0 eV in 26% Pt, 6.2 eV in 45% Pt, and 7.5 eV in 62% Pt. We interpret the observed shift to higher energies as result of an overall increase in carrier concentration n , which is also reflected in the calculated total density of states (see Supplementary Material). The step-like transition in the range 0-52% Pt of the reduced plasma frequencies $\tilde{\omega}_p$ can be attributed to the observed crystallographic phase transition (Figure 1) that drastically alters the band-structure of the material. For 62% Pt, the measured $\tilde{\omega}_p$ increases significantly, pointing to an increased contribution of the secondary Pt-phase to the total physical properties. Using the general relation between the optical loss and the plasma frequency $(2/\pi) \int_0^\infty \omega \text{Im}(\epsilon) d\omega = \omega_p^{228}$, one can observe that also the measured optical loss (Figure 2b) features this phase transition, suggesting an overall increase in metallic

bonding in the material.

Having established the structural and optical properties of the Zr-Pt-N system, we now address the thermal stability of this new ternary TMN phase. Figure 3a shows a set of scanning electron micrographs obtained from the Zr-Pt-N with smallest Pt concentration, namely 1%. Up to 500 °C, the ZrPt_xN_y films show no morphological change. As-deposited films also exhibit comparable hardness to other ZrNs, particularly zirconium oxy-nitrides¹⁻³ (Figure 3b), and a reduced resistivity compared to ZrN films²⁹ (Figure 3c).

Histograms of the indentation data Figure 3e show generally Gaussian distributions of hardness with no apparent clustering or bimodal presentation both before and after annealing. The hardness peaks at 26 at% Pt (Figure 3b), which can be explained both by a shift from strengthening through Pt replacement of oxygen to soften from both the subsequent replacement of N with Pt and the growth of a Pt-rich phase. Figure 1e highlights the reduction of oxygen content to negligible levels with the incorporation of Pt. As Zr-O bonds require the occupation of antibonding states electronically, these bonds are inherently less stable than either Zr-N or Zr-Pt bonds and typically promote vacancy formation to help stabilize the lattice structure³¹. Pt_3Zr structures form highly stable bonds²³ which drive preferential incorporation of Pt over Zr-O bonds and mechanistically describes the strengthening effect observed. However, incorporation of Pt onto the N sites (detailed in Sup-

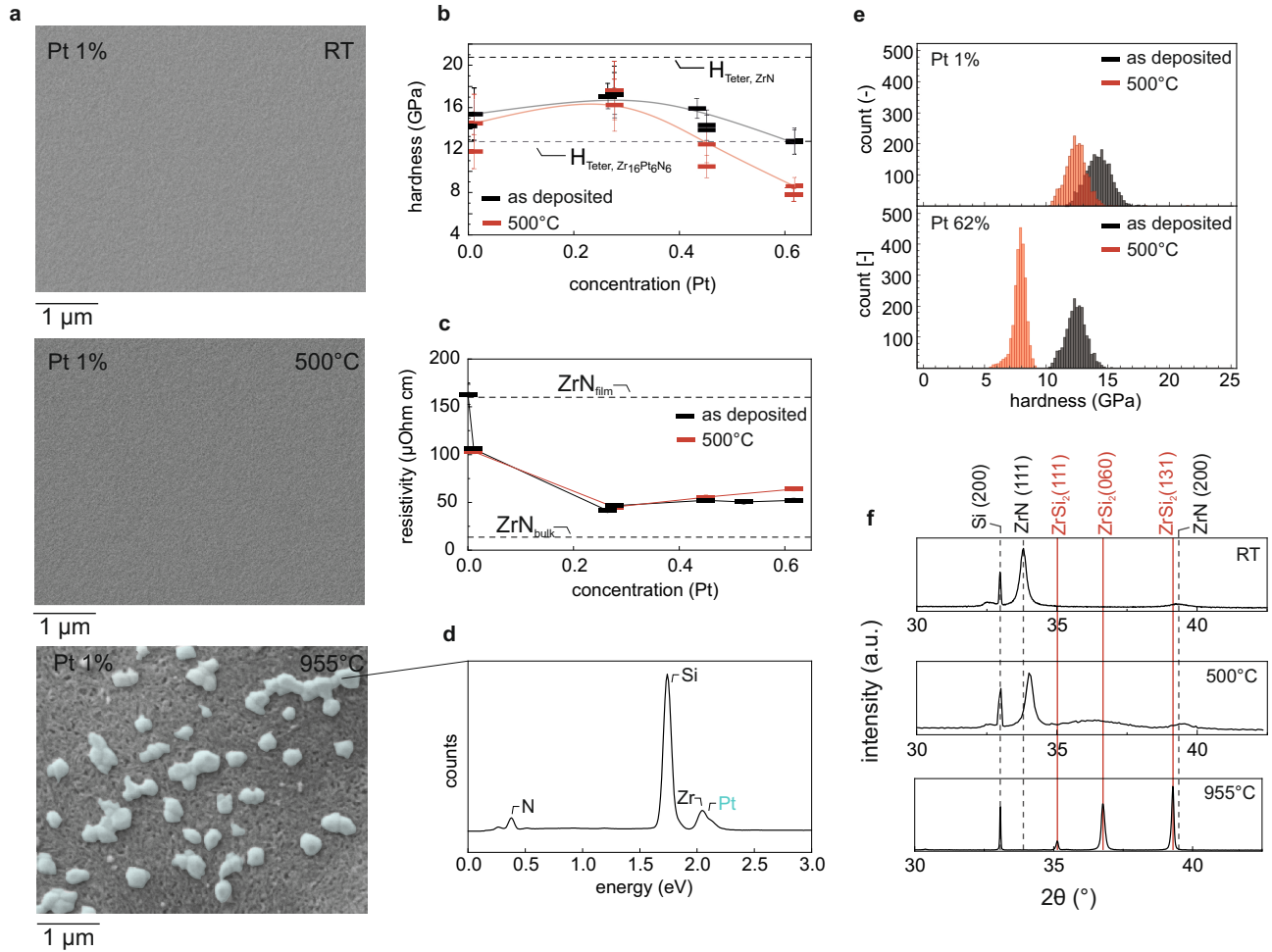


FIG. 3. Hardness, Resistivity, and Thermal Stability. (a) SEM images of a 1% Pt film at room temperature, 500 °C, and 955 °C. Pt precipitates are false-colored in blue. (b) Nanoindentation hardness of films as a function of Pt for room temperature (black) and 500 °C (red). Comparison made to reference Teter hardness values for ZrN and $Zr_{16}Pt_6N_6$ estimated from DFT calculations. (c) Resistivity of films as a function of Pt concentration for room temperature (black) and 500 °C (red) as compared to both film²⁹ and bulk³⁰ resistivity of ZrN. (d) EDS spectra highlighting the presence of Pt in SEM image of the 955 °C annealed sample. (e) Histograms of nanoindentation data for 1% Pt film (top) and 62% Pt film (bottom) both as deposited (black) and after annealing at 500 °C (red). (f) XRD spectra for 1% Pt at room temperature, 500 °C, and 955 °C.

plementary) reduce the hardness as compared to pure ZrN and the emergence of a nanoscale Pt-rich phase observed (Figure 1b) act as softening mechanism. Since Pt's hardness ($H_v = 9.4 \text{ GPa}$ ³²) is lower than $ZrPt_xN_y$, the nanoscale Pt-rich nuclei lower the film's average hardness and create localized opportunities for deformation.

While resistivity remains unaffected (Figure 3c) at 500 °C, clear structural degradation has begun and by 955 °C, chemical and structural decomposition is visible (Figure 3a, d, f). Precipitate formation on the film's surface (false-colored blue) is confirmed to be Pt particles by EDS (Figure 3d). Furthermore, XRD measurements emphasize the structural degradation into a mixture of Pt, Si from the substrate, and $ZrSi_2$ phases which are only present above 500 °C (Figure 3f). The mechanical degradation can also be explained by formation and growth of the Pt-rich phase. While surface precipitation of large Pt-rich particles is observed when annealed at 900 °C

(Figure 3a), these phases likely nucleate within the film at lower temperatures. This destabilization of the $ZrPt_xN_y$ films does not impact the dominant metallic bonding character and thus does not influence the observed electrical behavior.

This evidence for phase segregation and low thermal stability in $ZrPt_xN_y$ ternary alloys stand in contrast to DFT calculated stability maps¹⁶. Critically, we observe a solid state reaction between Pt-containing ZrN and the Si substrate when annealed at 900 °C (Figure 3f). This reaction completely consumes the ZrN phase and forms a crystalline $ZrSi_2$. While pure films of Zr and Si can react at 500-600 °C^{33,34}, ZrN-Si interfaces are stable up to 900 °C^{35,36}. As shown by XRD in both Figure 1b and 3f, 1% Pt films are structurally ZrN with incorporated Pt defects in the rocksalt lattice structure. Thus the complete conversion of the film to a $ZrSi_2$ phase at 900 °C underscores Pt's key role in destabilizing the ZrN structure and catalyzing the solid-state Zr-Si reaction. This decomposi-

tion of the ZrPt_xN_y film emphasizes its metastability.

Together these experiments emphasize the dominance of Zr-Pt metallic bonding in Zr-Pt-N alloys. It drives the formation of the metastable ZrPt_xN_y films through substitution of Pt on the N sublattice and transformation to a large, open unit cell structure. When extending to the design of other ternary TMNs, it is important to consider the metal-metal interactions in comparison to the parent metal nitride bonds. While DFT sets a key basis for establishing promising directions for ternary TMN design, this work emphasizes the critical role of experimental validation and investigation to fully identify destabilizing factors and address feasibility of ternary metal nitrides for functional applications.

- ¹Q. Meng, M. Wen, C. Hu, S. Wang, K. Zhang, J. Lian, and W. Zheng, "Influence of the residual stress on the nanoindentation-evaluated hardness for zirconiumnitride films," *Surface and Coatings Technology* **206**, 3250–3257 (2012).
- ²A. Z. M. S. E. S. P.-C. A. I. M. H. Staia, A. Trocelis and A. Montagne, "Assessment of the mechanical and tribological performance of a zrn pvd coating," *Surface Engineering* **35**, 491–500 (2019), <https://doi.org/10.1080/02670844.2017.1414766>.
- ³H.-M. Tung, J.-H. Huang, D.-G. Tsai, C.-F. Ai, and G.-P. Yu, "Hardness and residual stress in nanocrystalline zrn films: Effect of bias voltage and heat treatment," *Materials Science and Engineering: A* **500**, 104–108 (2009).
- ⁴H. A. Jehn, J.-H. Kim, and S. Hofmann, "Composition and properties of transition metal nitride thin films (zrxn, nbxn, monx)," *Surface and Coatings Technology* **36**, 715–727 (1988).
- ⁵H. A. Wriedt and J. L. Murray, "The n-ti (nitrogen-titanium) system," *Bulletin of Alloy Phase Diagrams* **8**, 378–388 (1987).
- ⁶A. Boltasseva and H. A. Atwater, "Low-loss plasmonic metamaterials," *Science* **331**, 290–291 (2011).
- ⁷J. Adachi, K. Kurosaki, M. Uno, and S. Yamanaka, "Thermal and electrical properties of zirconium nitride," *Journal of alloys and compounds* **399**, 242–244 (2005).
- ⁸A. Münster, K. Sagel, and G. Schlamp, "Titanium nitride and titanium carbide as semiconductors," *Nature* **174**, 1154 (1954).
- ⁹Y. Yuan, J. Wang, S. Adimi, H. Shen, T. Thomas, R. Ma, J. P. Attfield, and M. Yang, "Zirconium nitride catalysts surpass platinum for oxygen reduction," *Nature Materials* **19**, 282–286 (2020).
- ¹⁰J. Ban, H. Xu, G. Cao, Y. Fan, W. K. Pang, G. Shao, and J. Hu, "Synergistic effects of phase transition and electron-spin regulation on the electrocatalysis performance of ternary nitride," *Advanced Functional Materials* **33**, 2300623 (2023), <https://onlinelibrary.wiley.com/doi/pdf/10.1002/adfm.202300623>.
- ¹¹J. de Rojas, A. Quintana, G. Rius, C. Stefani, N. Domingo, J. L. Costa-Krämer, E. Menéndez, and J. Sort, "Voltage control of magnetism with magneto-ionic approaches: Beyond voltage-driven oxygen ion migration," *Applied Physics Letters* **120**, 070501 (2022), https://pubs.aip.org/aip/apl/article-pdf/doi/10.1063/5.0079762/19801386/070501_1_online.pdf.
- ¹²R. Potjan, M. Wislicenus, O. Ostien, R. Hoffmann, M. Lederer, A. Reck, J. Emara, L. Roy, B. Lilienthal-Uhlig, and J. Wosnitza, "300nm CMOS-compatible superconducting HfN and ZrN thin films for quantum applications," *Applied Physics Letters* **123**, 172602 (2023), https://pubs.aip.org/aip/apl/article-pdf/doi/10.1063/5.0176060/18189744/172602_1_5.0176060.pdf.
- ¹³R. Woods-Robinson, V. Stevanović, S. Lany, K. N. Heinselman, M. K. Horton, K. A. Persson, and A. Zakutayev, "Role of disorder in the synthesis of metastable zinc zirconium nitrides," *Phys. Rev. Mater.* **6**, 043804 (2022).
- ¹⁴V. Schnabel, R. Spolenak, M. Doebeli, and H. Galinski, "Structural color sensors with thermal memory: Measuring functional properties of ti-based nitrides by eye," *Advanced Optical Materials* **6**, 1800656 (2018), <https://onlinelibrary.wiley.com/doi/pdf/10.1002/adom.201800656>.
- ¹⁵A. Jain, G. Hautier, C. J. Moore, S. Ping Ong, C. C. Fischer, T. Mueller, K. A. Persson, and G. Ceder, "A high-throughput infrastructure for density functional theory calculations," *Computational Materials Science* **50**, 2295–2310 (2011).
- ¹⁶W. Sun, C. Bartel, E. Arca, S. Bauers, B. Matthews, B. Orvañanos, B. Chen, M. Toney, L. Schelhas, W. Tumas, J. Tate, A. Zakutayev, S. Lany, A. Holder, and G. Ceder, "A map of the inorganic ternary metal nitrides," *Nature Materials* **18**, 732–739 (2019).
- ¹⁷M. Chisaka, A. Ishihara, H. Morioka, T. Nagai, S. Yin, Y. Ohgi, K. Matsuzawa, S. Mitsushima, and K.-i. Ota, "Zirconium oxynitride-catalyzed oxygen reduction reaction at polymer electrolyte fuel cell cathodes," *ACS Omega* **2**, 678–684 (2017), <https://doi.org/10.1021/acsomega.6b00555>.
- ¹⁸M. Chisaka, Y. Yamamoto, N. Itagaki, and Y. Hattori, "Active site formation for oxygen reduction reaction on carbon-support-free titanium oxynitride with boosted activity in acidic media," *ACS Applied Energy Materials* **1**, 211–219 (2018), <https://doi.org/10.1021/acsaeam.7b00100>.
- ¹⁹M. Kilo, M. A. Taylor, G. Borchardt, I. Kaiser-Bischoff, H. Boysen, C. Rödel, and M. Lerch, "Fast anion-conduction in oxynitrides: Oxygen and nitrogen transport in (y, zr)-(o, n)," *Diffusion fundamentals* **8**, 8–1 (2008), <https://aflow.org/material/?id=afLOW:2fb74561ffd344ed>, <https://aflow.org/material/?id=afLOW:2fb74561ffd344ed>.
- ²⁰P. Giannozzi, S. Baroni, N. Bonini, M. Calandra, R. Car, C. Cavazzoni, D. Ceresoli, G. L. Chiarotti, M. Cococcioni, I. Dabo, A. Dal Corso, S. De Gironcoli, S. Fabris, G. Fratesi, R. Gebauer, U. Gerstmann, C. Gougousis, A. Kokalj, M. Lazzeri, L. Martin-Samos, N. Marzari, F. Mauri, R. Mazzarello, S. Paolini, A. Pasquarello, R. Paulatto, C. Sbraccia, S. Scandolo, G. Sclauzero, A. P. Seitsonen, A. Smogunov, P. Umari, and R. M. Wentzcovitch, "QUANTUM ESPRESSO: A modular and open-source software project for quantum simulations of materials," *Journal of Physics Condensed Matter* **21** (2009), 10.1088/0953-8984/21/39/395502.
- ²²G. Schatz and A. Weidinger, "Ionenstrahlanalytik," in *Nukleare Festkörperphysik: Kernphysikalische Meßmethoden und ihre Anwendungen* (Vieweg+Teubner Verlag, Wiesbaden, 1992) pp. 258–305.
- ²³H. Wang and E. A. Carter, "Metal-metal bonding in engle-brewer intermetallics: "anomalous" charge transfer in zirconium-platinum (zrpt3)," *Journal of the American Chemical Society* **115**, 2357–2362 (1993), <https://doi.org/10.1021/ja00059a034>.
- ²⁴C. G. Ribbing and A. Roos, "zirconium nitride (zrn) hafnium nitride (hfn)," in *Handbook of Optical Constants of Solids*, edited by E. D. Palik (Academic Press, Burlington, 1997) pp. 351–369.
- ²⁵G. V. Naik, V. M. Shalaev, and A. Boltasseva, "Alternative plasmonic materials: Beyond gold and silver," *Advanced Materials* **25**, 3264–3294 (2013), <https://onlinelibrary.wiley.com/doi/pdf/10.1002/adma.201205076>.
- ²⁶M. Kumar, S. Ishii, N. Umezawa, and T. Nagao, "Band engineering of ternary metal nitride system ti1-x zrxn for plasmonic applications," *Opt. Mater. Express* **6**, 29–38 (2016).
- ²⁷A. B. Kuzmenko, "Kramers-Kronig constrained variational analysis of optical spectra," *Review of Scientific Instruments* **76**, 083108 (2005), https://pubs.aip.org/aip/rsi/article-pdf/doi/10.1063/1.1979470/16127359/083108_1_online.pdf.
- ²⁸F. Bassani, G. P. Parravicini, R. A. Ballinger, and J. L. Birman, "Electronic states and optical transitions in solids," (American Institute of Physics, 1976) Chap. Chapter 5.
- ²⁹M. A. Signore, D. Valerini, A. Rizzo, L. Tapfer, L. Capodieci, and A. Cappello, "Investigation of the physical properties of ion assisted zrn thin films deposited by rf magnetron sputtering," *Journal of Physics D: Applied Physics* **43**, 225401 (2010).
- ³⁰C. C. Wang, S. A. Akbar, W. Chen, and V. D. Patton, "Electrical properties of high-temperature oxides, borides, carbides, and nitrides," *Journal of Materials Science* **30**, 1627–1641 (1995).
- ³¹C. Schwandt and W. Weppner, "Kinetics of oxygen, platinum/stabilized zirconia and oxygen, gold/stabilized zirconia electrodes under equilibrium conditions," *J. Electrochem. Soc.* **144**, 3728–3738 (1997).
- ³²R. Farraro and R. B. Mclellan, "Temperature dependence of the young's modulus and shear modulus of pure nickel, platinum, and molybdenum," *Metallurgical Transactions A* **8**, 2357–2362 (1977), <https://doi.org/10.1007/BF02644859>.
- ³³T. Yamauchi, S. Zaima, K. Mizuno, H. Kitamura, Y. Koide, and Y. Yasuda, "Solid-phase reactions and crystallographic structures in Zr/Si systems," *Journal of Applied Physics* **69**, 7050–7056 (1991), <https://pubs.aip.org/aip/jap/article>

- pdf/69/10/7050/18642652/7050_1_online.pdf.
- ³⁴H. Tanaka, T. J. Konno, R. Sinclair, and N. Hirashita, "Interfacial reactions in the Zr-Si system studied by in-situ transmission electron microscopy," *Journal of Applied Physics* **78**, 4982–4987 (1995), https://pubs.aip.org/aip/jap/article-pdf/78/8/4982/18679152/4982_1_online.pdf.
- ³⁵J.-L. Ruan, D.-F. Lii, J. Chen, and J.-L. Huang, "Investigation of substrate bias effects on the reactively sputtered zrn diffusion barrier films," *Ceramics International* **35**, 1999–2005 (2009).
- ³⁶M. B. Takeyama, A. Noya, and K. Sakanishi, "Diffusion barrier properties of ZrN films in the Cu/Si contact systems," *Journal of Vacuum Science & Technology B: Microelectronics and Nanometer Structures Processing, Measurement, and Phenomena* **18**, 1333–1337 (2000), https://pubs.aip.org/avs/jvb/article-pdf/18/3/1333/8204409/1333_1_online.pdf.